

A Hybrid Model for Electromagnetic Leakage from an Apertured Complex Metallic Enclosures

Yan-Fei Gong*, Jian-Hong Hao, Lu-Hang Jiang, and Jie-Qing Fan

Abstract—An efficient and accurate hybrid model has been developed for the electromagnetic leakage from two apertured cascaded metallic rectangular enclosures connected by a metallic plate with an aperture covered by a non-magnetic conductive sheet excited by an electric dipole located in the enclosure. The leakage fields through the covered aperture are derived by using the dyadic Green's function and employing the approximate boundary conditions at both sides of the sheet which is regarded as an infinite conductive plate. Then, the leakage fields into the external space through the aperture regardless of its thickness at the end of the enclosure are derived based on a generalization of the method of moments (MoM). Finally, the shielding effectiveness (SE) at the target points outside the enclosure is calculated for the intermediate analysis of the leakage fields. Comparison with the full wave simulation software CST has verified the model over a wide frequency band. The hybrid model then is employed to analyze the effect of different factors including the thickness and the conductivity of the conductive sheet on the SE, and the corresponding physical mechanisms of the leakage fields are also illuminated. The hybrid model can also be extended to deal with other cases, including the whole plate made of non-magnetic conductive material without apertures, the infinite thickness of the aperture at the end of the enclosure, and the aperture at the end of the enclosure also covered by a non-magnetic conductive sheet.

1. INTRODUCTION

Due to the increasing complexity and density of high speed integrated circuits and electronic devices, the problems of electromagnetic interference (EMI) have become considerably common and severe. Electromagnetic shielding, one of the primary technical measures for suppressing the EMI via field coupling channel, has been widely used in the electromagnetic compatibility (EMC) design [1–3]. It can be simply implemented by encasing vulnerable circuits and components within a metallic box to protect them from the EMI. However, it is inevitable that the enclosure contains apertures in the internal regions and on its surface due to the needs for the installation of lines, ventilation and heat dissipation, etc., which may cause significant electromagnetic leakage into the internal adjacent regions of the enclosure and the external environment through slots and apertures, and degrading its shielding effectiveness (SE) dramatically as well as having a substantial influence on the surrounding environment. Designing an enclosure of better shielding effect has always been an important issue [4–7]. Recently, the internal structures of the enclosure have become considerably complex with the increase of integration of electronic devices, thus studying the SE of various complicated metallic shielding enclosures provides guidance of great importance for electromagnetic shielding theory and practical electromagnetic protection technology. Considerable work has been done in the study of the SE of a metallic rectangular enclosure with apertures using numerical methods [4], analytical methods [5, 6], and hybrid methods [7]. Numerical methods, including the finite difference time domain (FDTD)

Received 10 October 2016, Accepted 25 March 2017, Scheduled 13 April 2017

* Corresponding author: Yan-Fei Gong (yuxin880323@126.com).

The authors are with the Department of Electrical and Electronic Engineering, North China Electric Power University, Beijing, China.

method, finite element method (FEM), method of moments (MoM), and transmission-line modeling (TLM) method, are robust and accurate, but require large computational resources because of the detailed mesh generation for complicated electronic systems. As a result, analytical approaches such as Bethe's small aperture coupling theory, equivalent circuit method and BLT equation, which are much faster and more convenient in the analysis of the effect of different parameters on the SE, have been especially used in evaluating the SE of the target points. Hybrid methods, which combine the merits of numerical and analytical methods, have the advantages of substantially reducing the computer memory and the processing time, overcoming some limitations of single methods, etc. on the premise that the computational accuracy is guaranteed. The electromagnetic leakage of an apertured rectangular aperture excited by an internal electric dipole has been studied based on the Bethe's small aperture coupling theory in [8, 9], and the SE is used to intermediately measure the electromagnetic leakage. The small aperture model is reliable in terms of calculation accuracy but restricted to the condition that the size of the aperture is shorter than $1/10$ wavelength of interest and that the thickness of the enclosure is neglected. In order to overcome these limitations, Dehkhoda et al. [17] have introduced a generalized model MoM to evaluate the SE of an apertured enclosure with an finite wall thickness exposed to a plane wave of normal incidence. In this method, the unknown magnetic currents at both sides of the rectangular aperture are represented by the sinusoidal basis functions. By employing the surface equivalence principle and boundary conditions at each of the apertures, the unknown magnetic currents then are obtained and therefore the electric fields inside the enclosure.

With the rapid development of material science and technology, an increasing number of compound conductive materials with good flexibility and low weight have been used in the design of shielding enclosures [10, 11]. Sometimes, they are employed to close unnecessary apertures to decrease the electromagnetic leakage from them, and improve the SE of the enclosures [12]. Konefal et al. [13] have implemented the intermediate level circuit model to calculate the SE of a metallic rectangular enclosure with an aperture covered by a conductive sheet against a normally incident plane wave. However, this model is restricted to the rectangular aperture and plane wave of a normal incidence; therefore, it will become more complicated and time-consuming, and even fail in other cases.

Previous work mainly focuses on an apertured single enclosure. In fact, a complex metallic enclosure is generally divided into multiple spatial regions, and thus it is worthwhile to investigate the complicated mutual EMI of different nearby regions. In this paper, an efficient and accurate hybrid model is proposed for predicting the electromagnetic leakage field coupling through apertures of multiple cascaded rectangular enclosures connected by a metallic plate with a covered aperture, and the excitation source is an electric dipole located inside the enclosure. In order to calculate the leakage fields outside the enclosures, first, we derive the equivalent magnetic current on the right surface of the sheet by using the electromagnetic fields excited by the dipole with the aperture short-circuited and employing the approximate boundary conditions at both sides of the sheet which is regarded as an infinite conductive plate. Then, using the cavity Green's function and the equivalent magnetic current, the leakage fields inside the enclosure through the covered aperture are obtained. Finally, the leakage fields outside the enclosures through the aperture of which the thickness is very small are calculated based on the generalized model MoM. Overcoming the above limitations of the intermediate level circuit method, this model is appropriate for arbitrary covered aperture shape and arbitrary source, because the equivalent surface magnetic of the sheet plays the part of source in calculating the leakage fields inside the enclosure.

A good agreement over a broad frequency range up to 3 GHz is observed between the results of the hybrid model and the full-wave simulation software CST which is based on the TLM method for the covered rectangular aperture and the covered square annular aperture respectively. Then, the hybrid model is employed to analyze the effect of different factors including the thickness and conductivity of the sheet on the SE. The hybrid model can also be extended to deal with other cases, including the whole plate made of non-magnetic conductive material without apertures, finite thickness of the aperture at the end of the enclosure and the aperture at the end of the enclosure covered by a non-magnetic conductive sheet. There is a good agreement between the hybrid results in the three extended cases and the CST results up to 3 GHz. In addition, the effect of the three extended cases on the SE is compared with that of the original case; the reason and mechanism which cause it are also illuminated.

2. THEORY

2.1. Hybrid Model

The geometry of the hybrid model is shown in Figure 1(a). It consists of two cascaded metallic rectangular enclosures (enclosure 1 and enclosure 2) connected by a metallic plate with a rectangular aperture (aperture 1) of size $l_1 \times w_1$ covered by a non-magnetic conductive sheet of thickness d_1 , conductivity σ_1 , electric permittivity ε_1 ($\varepsilon_1 = \varepsilon_0$, ε_0 is the electric permittivity of vacuum), and magnetic permeability μ_1 ($\mu_1 = \mu_0$, μ_0 is the magnetic permeability of vacuum). There is also a rectangular aperture (aperture 2) of size $l_2 \times w_2$ on the right wall of enclosure 2, and a very small wall thickness of the two enclosures is chosen. It is assumed that the enclosure wall and metallic plate are perfectly conductive. The dimensions of the two enclosures are both $x_e \times y_e \times z_e$, respectively. The center points of aperture 1 and aperture 2 are located at (x_1, y_1, z_1) and (x_2, y_2, z_2) , respectively. The interference source is a y -oriented electric dipole with a moment of $I \cdot dl$, and located at (x_s, y_s, z_s) in the enclosure 1. The observation point is located at (x, y, z) . Figure 1(b) shows the side view of the hybrid model which is divided into three regions: region I (II) is the volume inside enclosure 1(2), and region III represents the half free space outside the enclosures.

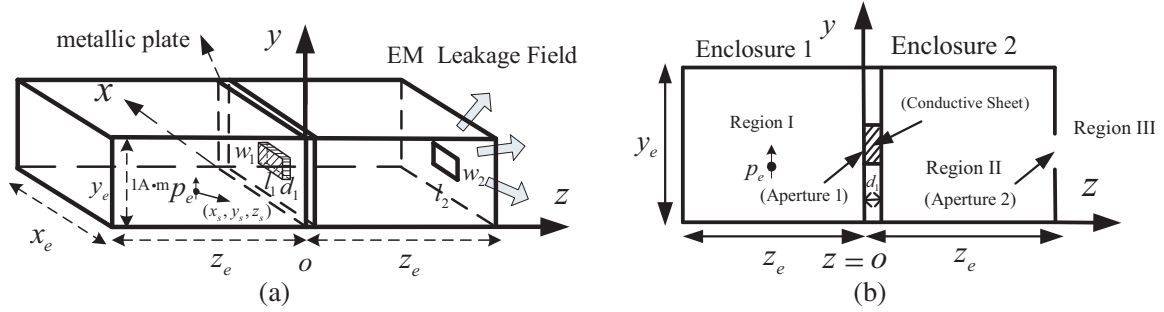


Figure 1. (a) The geometry of the hybrid model when aperture 2 is zero thickness. (b) The corresponding side view of (a).

According to Reference [14], the electric fields E^I inside enclosure 1 (region I) with the aperture short-circuited produced by the y -directed electric dipole has been known. By using the Faraday's electromagnetic induction law $\nabla \times E^I = -j\omega H^I$, the x -component and y -component of the corresponding magnetic field in region I can be obtained as

$$H_x^I(x, y, z) = \frac{-Idl}{x_e y_e z_e} \sum_{m=0}^{\infty} \sum_{l=0}^{\infty} \Gamma_{ml} \left(\frac{y_e}{2k_1} \right) \sin^{-1}(k_1 y_e) \times \{ \cos k_1 (y + y_s - y_e) + \cos k_1 (|y - y_s| - y_e) \} \quad (1)$$

$$H_y^I(x, y, z) = 0 \quad (2)$$

where I and dl are the current and length of the electric dipole, respectively; m and l are the mode index numbers of the enclosure 1 along the x -axis and the z -axis, respectively, and

$$k_1 = \sqrt{k_0^2 - (m\pi/x_e)^2 - (l\pi/z_e)^2} \quad (3)$$

$$\Gamma_{ml} = \varepsilon_{0m} \varepsilon_{0l} \left(\frac{l\pi}{z_e} \right) \cos \left(\frac{l\pi z}{z_e} \right) \sin \left(\frac{l\pi z_s}{z_e} \right) \sin \left(\frac{m\pi x}{x_e} \right) \sin \left(\frac{m\pi x_s}{x_e} \right) \quad (4)$$

where k_0 is the wave number in vacuum, and $\varepsilon_{0m}(\varepsilon_{0l}) = 1$ for $m(l) = 0, = 2$ for $m(l) \neq 0$.

2.2. Electromagnetic Leakage Fields in Region II

The electromagnetic leakage fields inside enclosure 2 (region II) in terms of the electric vector potential A_{m1}^{II} are given as [15]

$$\mathbf{E}^{\text{II}} = -\frac{1}{\varepsilon_0} \nabla \times \mathbf{A}_{m1}^{\text{II}} \quad (5)$$

$$\mathbf{H}^{\text{II}} = -\frac{-j\omega}{k_0^2} (k_0^2 \mathbf{A}_{m1}^{\text{II}} + \nabla (\nabla \cdot \mathbf{A}_{m1}^{\text{II}})) \quad (6)$$

where ω is the angular frequency, ε_0 is the permittivity in vacuum, and A_{m1}^{II} satisfies the inhomogeneous wave equation

$$\nabla^2 \mathbf{A}_{m1}^{\text{II}} + k_0^2 \mathbf{A}_{m1}^{\text{II}} = -\varepsilon_0 M_1 \quad (7)$$

where M_1 denotes the equivalent magnetic current on the right surface ($z = d_1$ plane) of the sheet, and thus only has x - and y -components.

Using the surface equivalence principle and the image theory, the covered aperture can be replaced by the equivalent surface magnetic current M_1 of

$$\begin{aligned} M_1 &= 2 (E_{ty}^{\text{II}} e_y + E_{tx}^{\text{II}} e_x) \times e_z \\ &= 2E_{ty}^{\text{II}} e_x - 2E_{tx}^{\text{II}} e_y \\ &= M_{1x} e_x + M_{1y} e_y \end{aligned} \quad (8)$$

where E_{ty}^{II} and E_{tx}^{II} denote the y - and x -components of tangential electric fields on the $z = d_1$ plane, respectively. $M_{1x} = 2E_{ty}^{\text{II}}$, $M_{1y} = -2E_{tx}^{\text{II}}$.

E_{ty}^{II} and E_{tx}^{II} can be approximately obtained by employing boundary conditions at both sides ($z = 0$ plane and $z = d_1$ plane) of the sheet 1 and calculating the intrinsic transfer impedance $\eta(d_1)$ of it [16]. A relation then is established between E_{ty}^{II} (E_{tx}^{II}) and the relative tangential magnetic field components on the $z = 0$ plane using $\eta(d_1)$. Although Equation (9) is only valid for infinite sheets, it leads to acceptable results in our method.

Figure 2 shows the geometry of an infinite conductive sheet against a plane wave of normal incidence, considering that $\eta(d_1)$ is not relevant to the type of the source. When the plane wave in region I normally incidents upon the sheet 1, there will be a reflected wave in region I from the left surface of the sheet ($z = 0$ plane), and a transmitted wave in region II.

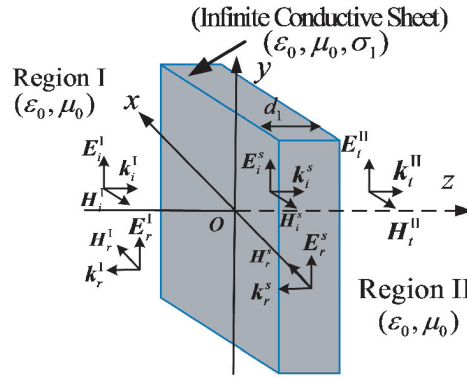


Figure 2. The geometry of an infinite conductive sheet against a plane wave of normal incidence.

$$\begin{cases} E_{ty}^{\text{II}} = \eta(d_1) H_{tx}^{\text{I}} \\ E_{tx}^{\text{II}} = -\eta(d_1) H_{ty}^{\text{I}} \\ \eta(d_1) = (-2\eta_1 \eta_s) / [(\eta_1 + \eta_s) e^{jk_s d_1} - (\eta_1 - \eta_s) e^{-jk_s d_1}] \end{cases} \quad (9)$$

where H_{tx}^I and H_{ty}^I denote the x - and y -components of tangential magnetic fields on the $z = 0$ plane, respectively. $\eta_1 = \sqrt{\mu_0/\varepsilon_0}$, $k_s = \omega\sqrt{\mu_0\varepsilon_s}$, $\varepsilon_s = \varepsilon_0 - j(\sigma_1/\omega)$, $\eta_s = \sqrt{\mu_0/\varepsilon_s}$.

Here, we use the corresponding H_x^I and H_y^I obtained in Section 2.1 instead of H_{tx}^I and H_{ty}^I , so E_{ty}^{II} and E_{tx}^{II} can be represented as

$$\begin{cases} E_{ty}^{II} = \eta(d_1)H_x^I \\ E_{tx}^{II} = -\eta(d_1)H_y^I = 0 \end{cases} \quad (10)$$

By using $A_{m1}^{II} = \iint_{S'} \overline{\overline{G}}_m(r, r') \cdot M_1(r') ds'$, where $\overline{\overline{G}}_m(r, r')$ is the dyadic Green's function of region II; r and r' are, respectively, the observation and the equivalent magnetic current source vectors, and S' denotes the area where the sheet 1 covers, Equation (7) is substituted as

$$\nabla^2 \overline{\overline{G}}_m(r, r') + k_0^2 \overline{\overline{G}}_m(r, r') = -\varepsilon_0 \overline{\overline{I}} \delta(r - r') \quad (11)$$

where the unit dyad $\overline{\overline{I}} = e_x e_x + e_y e_y$.

According to Reference [17], the xx - and yy -components of $\overline{\overline{G}}_m(r, r')$ in Equation (11) can be written as

$$G_{mxx} = - \sum_{m'=0}^{\infty} \sum_{n'=0}^{\infty} \frac{\varepsilon_0 \varepsilon_{0m'} \varepsilon_{0n'}}{x_e y_e k_z} \sin(k_{xm'} x) \cos(k_{yn'} y) \sin(k_{xm'} x') \cos(k_{yn'} y') \frac{\cos(k_z(z - z_e))}{\sin(k_z(z_e - d_1))} \delta(z' - d_1) \quad (12)$$

$$G_{myy} = - \sum_{m'=0}^{\infty} \sum_{n'=0}^{\infty} \frac{\varepsilon_0 \varepsilon_{0m'} \varepsilon_{0n'}}{x_e y_e k_z} \cos(k_{xm'} x) \sin(k_{yn'} y) \cos(k_{xm'} x') \sin(k_{yn'} y') \frac{\cos(k_z(z - z_e))}{\sin(k_z(z_e - d_1))} \delta(z' - d_1) \quad (13)$$

where (m', n') are the mode index numbers of the region II; $k_{xm'} = m'\pi/x_e$, $k_{yn'} = n'\pi/y_e$, and $k_z = \sqrt{k_0^2 - k_{xm'}^2 - k_{yn'}^2}$; $\varepsilon_{0m'}$, $\varepsilon_{0n'}$ are the Neumann's Numbers, and $\varepsilon_{0m'}(\varepsilon_{0n'}) = 1$ for $m'(n') = 0$, $\varepsilon_{0m'}(\varepsilon_{0n'}) = 2$ for $m'(n') \neq 0$.

Substituting Equations (8), (10), (12) and (13) into the expression of the electric vector potential A_{m1}^{II} , the x - and y -components of it are obtained as

$$\begin{aligned} A_{m1}^{IIx} &= \iint_{S'} G_{mxx} M_{1x} ds' = -2\eta(d_1) \sum_{m'=0}^{\infty} \sum_{n'=0}^{\infty} \frac{-\varepsilon_0 \varepsilon_{0m'} \varepsilon_{0n'}}{x_e y_e k_z \sin(k_z(z_e - d_1))} \\ &\quad \times \iint_{S'} H_x^I(x', y', z') \sin(k_{xm'} x') \cos(k_{yn'} y') ds' \times \sin(k_{xm'} x) \cos(k_{yn'} y) \cos(k_z(z - z_e)) \quad (14) \end{aligned}$$

$$A_{m1}^{IIy} = \iint_{S'} G_{myy} M_{1y} ds' = 0 \quad (15)$$

The electromagnetic leakage fields in region II are then obtained from Equations (5) and (6) as

$$E_{M1}^{IIx} = 0 \quad (16)$$

$$\begin{aligned} E_{M1}^{IIy} &= -2\eta(d_1) \sum_{m'=0}^{\infty} \sum_{n'=0}^{\infty} \frac{\varepsilon_{0m'} \varepsilon_{0n'}}{x_e y_e \sin(k_z(z_e - d_1))} \sin(k_{xm'} x) \cos(k_{yn'} y) \sin(k_z(z - z_e)) \\ &\quad \times \iint_{S'} H_x^I(x', y', z') \sin(k_{xm'} x') \cos(k_{yn'} y') ds' \quad (17) \end{aligned}$$

$$\begin{aligned} E_{M1}^{IIz} &= -2\eta(d_1) \sum_{m'=0}^{\infty} \sum_{n'=0}^{\infty} \frac{\varepsilon_{0m'} \varepsilon_{0n'} k_{yn'}}{x_e y_e k_z \sin(k_z(z_e - d_1))} \sin(k_{xm'} x) \sin(k_{yn'} y) \cos(k_z(z - z_e)) \\ &\quad \times \iint_{S'} H_x^I(x', y', z') \sin(k_{xm'} x') \cos(k_{yn'} y') ds' \quad (18) \end{aligned}$$

$$\begin{aligned}
H_{M_1}^{\text{II}x} &= 2\eta(d_1) \frac{j\omega}{k_0^2} \sum_{m'=0}^{\infty} \sum_{n'=0}^{\infty} \frac{\varepsilon_0 \varepsilon_{0m'} \varepsilon_{0n'} (k_0^2 - k_{xm'}^2)}{x_e y_e k_z \sin(k_z(z_e - d_1))} \sin(k_{xm'} x) \cos(k_{yn'} y) \cos(k_z(z - z_e)) \\
&\quad \times \iint_{S'} H_x^1(x', y', z') \sin(k_{xm'} x') \cos(k_{yn'} y) ds' \tag{19}
\end{aligned}$$

$$\begin{aligned}
H_{M_1}^{\text{II}y} &= -2\eta(d_1) \frac{j\omega}{k_0^2} \sum_{m'=0}^{\infty} \sum_{n'=0}^{\infty} \frac{\varepsilon_0 \varepsilon_{0m'} \varepsilon_{0n'} k_{xm'} k_{yn'}}{x_e y_e k_z \sin(k_z(z_e - d_1))} \cos(k_{xm'} x) \sin(k_{yn'} y) \cos(k_z(z - z_e)) \\
&\quad \times \iint_{S'} H_x^1(x', y', z') \sin(k_{xm'} x') \cos(k_{yn'} y) ds' \tag{20}
\end{aligned}$$

$$\begin{aligned}
H_{M_1}^{\text{II}z} &= -2\eta(d_1) \frac{j\omega}{k_0^2} \sum_{m'=0}^{\infty} \sum_{n'=0}^{\infty} \frac{\varepsilon_0 \varepsilon_{0m'} \varepsilon_{0n'} k_{xm'}}{x_e y_e \sin(k_z(z_e - d_1))} \cos(k_{xm'} x) \cos(k_{yn'} y) \sin(k_z(z - z_e)) \\
&\quad \times \iint_{S'} H_x^1(x', y', z') \sin(k_{xm'} x') \cos(k_{yn'} y) ds' \tag{21}
\end{aligned}$$

2.3. Electromagnetic Leakage Fields in Region III

When the thickness of the aperture 2 is very small which can be seen as zero thickness, the tangential electric field of this rectangular aperture on $z = z_e$ plane can be represented by the following modal expansion [18]

$$\begin{aligned}
E_{\text{apt}} &= \sum_{p,q} A_{pq} \sin\left(\frac{p\pi}{l_2} \left(x + \frac{l_2}{2} - x_0\right)\right) \cos\left(\frac{q\pi}{w_2} \left(y + \frac{w_2}{2} - y_0\right)\right) e_y \\
&\quad + \sum_{p,q} B_{pq} \cos\left(\frac{p\pi}{l_2} \left(x + \frac{l_2}{2} - x_0\right)\right) \sin\left(\frac{q\pi}{w_2} \left(y + \frac{w_2}{2} - y_0\right)\right) e_x \tag{22}
\end{aligned}$$

where (p, q) are the mode index numbers of the aperture; A_{pq} and B_{pq} are the unknown amplitudes of the pq th mode.

According to the surface equivalence principle, aperture 2 can be replaced by the equivalent magnetic current of $M_2 = E_{\text{apt}} \times e_z$, so the equivalent magnetic current can be expressed as

$$M_2 = \sum_{p,q} A_{pq} \psi_{pq} e_x - \sum_{p,q} B_{pq} \varphi_{pq} e_y = M_{2x} e_x - M_{2y} e_y \tag{23}$$

where $\psi_{pq} = \sin\left(\frac{p\pi}{l_2} \left(x + \frac{l_2}{2} - x_0\right)\right) \cos\left(\frac{q\pi}{w_2} \left(y + \frac{w_2}{2} - y_0\right)\right)$, $\varphi_{pq} = \cos\left(\frac{p\pi}{l_2} \left(x + \frac{l_2}{2} - x_0\right)\right) \sin\left(\frac{q\pi}{w_2} \left(y + \frac{w_2}{2} - y_0\right)\right)$.

Using the magnetic dyadic Green's function $\overline{\overline{G}}_{HM}$ of region II, and the electromagnetic fields in region II generated by M_2 are given as

$$E_{M_2}^{\text{II}} = - \iint_S \nabla \times \overline{\overline{G}}_{HM} \cdot (-M_2) ds'' \tag{24}$$

$$H_{M_2}^{\text{II}} = -j\omega\varepsilon_0 \iint_S \nabla \times \overline{\overline{G}}_{HM} \cdot (-M_2) ds'' \tag{25}$$

According to Equation (25), the magnetic fields in region II can be obtained as

$$\begin{aligned}
H_{M_2}^{\text{II}x} &= -j\omega\varepsilon_0 \sum_{m'',n''} \frac{2(2 - \delta_{m''n''})}{x_e y_e k_0^2 k_z'' \sin(k_z''(z_e - d_1))} \left[(k_0^2 - k_{xm''}^2) \text{I}_x^{m''n''} - k_{xm''} k_{yn''} \text{I}_y^{m''n''} \right] \\
&\quad \times \sin(k_{xm''} x) \cos(k_{yn''} y) \cos(k_z'' z) \tag{26}
\end{aligned}$$

$$\begin{aligned}
H_{M_2}^{\text{II}y} &= -j\omega\varepsilon_0 \sum_{m'',n''} \frac{2(2 - \delta_{m''n''})}{x_e y_e k_0^2 k_z'' \sin(k_z''(z_e - d_1))} \left[-k_{xm''} k_{yn''} \text{I}_x^{m''n''} - (k_0^2 - k_{yn''}^2) \text{I}_y^{m''n''} \right] \\
&\quad \times \cos(k_{xm''} x) \sin(k_{yn''} y) \cos(k_z'' z) \tag{27}
\end{aligned}$$

$$H_{M_2}^{IIz} = j\omega\epsilon_0 \sum_{m'',n''}^{\infty} \frac{2(2 - \delta_{m''n''})}{x_e y_e k_0^2 \sin(k_z''(z_e - d_1))} \left[k_{xm''} I_x^{m''n''} + k_{yn''} I_y^{m''n''} \right] \times \cos(k_{xm''}x) \cos(k_{yn''}y) \sin(k_z''z) \quad (28)$$

where $k_{xm''} = m''\pi/x_e$, $k_{yn''} = n''\pi/y_e$, and $k_z'' = \sqrt{k_0^2 - k_{xm''}^2 - k_{yn''}^2}$; $\delta_{m''n''} = \begin{cases} 1, & m'' \text{ or } n'' = 0, \\ 0, & \text{else.} \end{cases}$; $I_x^{m''n''} = \iint_S M_{2x}(x'', y) \sin(k_{xm''}x'') \cos(k_{yn''}y'') ds''$; $I_y^{m''n''} = \iint_S M_{2y}(x'', y'') \cos(k_{xm''}x'') \sin(k_{yn''}y'') ds''$.

The electromagnetic leakage fields in region III can be calculated by the scattered electromagnetic fields generated by the equivalent magnetic current M_2

$$E_{M_2}^{IIIx} = \frac{-1}{4\pi^2} \sum_{p,q} B_{pq} \int_{-\infty}^{+\infty} \int_{-\infty}^{+\infty} \varphi'_{pq} e^{-jk_z''|z-z''|} e^{j(k_{xm''}x+k_{yn''}y)} dk_{xm''} dk_{yn''} \quad (29)$$

$$E_{M_2}^{IIIy} = \frac{1}{4\pi^2} \sum_{p,q} A_{pq} \int_{-\infty}^{+\infty} \int_{-\infty}^{+\infty} \psi'_{pq} e^{-jk_z''|z-z''|} e^{j(k_{xm''}x+k_{yn''}y)} dk_{xm''} dk_{yn''} \quad (30)$$

$$E_{M_2}^{IIIz} = -\frac{1}{4\pi^2} \sum_{p,q} \int_{-\infty}^{+\infty} \int_{-\infty}^{+\infty} \frac{(B_{pq}k_{xm''}\varphi'_{pq} - A_{pq}k_{yn''}\psi'_{pq})}{k_z''} e^{-jk_z''|z-z''|} e^{j(k_{xm''}x+k_{yn''}y)} dk_{xm''} dk_{yn''} \quad (31)$$

$$H_{M_2}^{IIIx} = \frac{\omega\epsilon_0}{4\pi^2 k_0^2} \sum_{p,q} \int_{-\infty}^{+\infty} \int_{-\infty}^{+\infty} \frac{A_{pq}\psi'_{pq}(k_{xm''}^2 - k_0^2) + B_{pq}k_{xm''}k_{yn''}\varphi'_{pq}}{k_z''} e^{-jk_z''|z-z''|} e^{j(k_{xm''}x+k_{yn''}y)} dk_{xm''} dk_{yn''} \quad (32)$$

$$H_{M_2}^{IIIy} = \frac{\omega\epsilon_0}{4\pi^2 k_0^2} \sum_{p,q} \int_{-\infty}^{+\infty} \int_{-\infty}^{+\infty} \frac{A_{pq}k_{xm''}k_{yn''}\varphi'_{pq} + B_{pq}\psi'_{pq}(k_{yn''}^2 - k_0^2)}{k_z''} e^{-jk_z''|z-z''|} e^{j(k_{xm''}x+k_{yn''}y)} dk_{xm''} dk_{yn''} \quad (33)$$

$$H_{M_2}^{IIIz} = \frac{\omega\epsilon_0}{4\pi^2 k_0^2} \sum_{p,q} \int_{-\infty}^{+\infty} \int_{-\infty}^{+\infty} (A_{pq}k_{xm''}\varphi'_{pq} + B_{pq}\psi'_{pq}k_{yn''}) e^{-jk_z''|z-z''|} e^{j(k_{xm''}x+k_{yn''}y)} dk_{xm''} dk_{yn''} \quad (34)$$

where $\psi'_{pq} = \iint_S \psi_{pq} e^{-j(k_{xm''}x+k_{yn''}y)} dk_{xm''} dk_{yn''}$, $\varphi'_{pq} = \iint_S \varphi_{pq} e^{-j(k_{xm''}x+k_{yn''}y)} dk_{xm''} dk_{yn''}$.

In order to determine the coefficients M_{2x} and M_{2y} of the equivalent magnetic current M_2 , we apply the continuity of tangential magnetic field at $z = z_e$ plane

$$H_{M_1}^{IIx}|_{z=z_e} + H_{M_2}^{IIx}|_{z=z_e} = H_{M_2}^{IIIx}|_{z=z_e} \quad (35)$$

$$H_{M_1}^{IIy}|_{z=z_e} + H_{M_2}^{IIy}|_{z=z_e} = H_{M_2}^{IIIy}|_{z=z_e} \quad (36)$$

For Equations (35) and (36), we choose $\psi_{p'q'}$ and $\varphi_{p'q'}$ as the testing functions separately, and use Galerkin's method to calculate equations

$$I_{xp'q'} = \sum_{p,q}^{\infty} (A_{pq} Y_{pp'q'}^{aa} + B_{pq} Y_{pp'q'}^{ab}) \quad (37)$$

$$I_{yp'q'} = \sum_{p,q}^{\infty} (A_{pq} Y_{pp'q'}^{ba} + B_{pq} Y_{pp'q'}^{bb}) \quad (38)$$

where $I_{xp'q'} = \iint_S H_{M_1}^{IIx} \psi_{p'q'} ds''$, $I_{yp'q'} = \iint_S H_{M_1}^{IIy} \varphi_{p'q'} ds''$; the admittance coefficients $Y_{pp'q'}^{aa}$, $Y_{pp'q'}^{ab}$, $Y_{pp'q'}^{ba}$ and $Y_{pp'q'}^{bb}$ can be represented according to some related functions, where $I_{xppm''n''} = \iint_S \psi_{pq} \sin(k_{xm''}) \cos(k_{yn''}) dx'' dy''$; $I_{yppm''n''} = \iint_S \varphi_{pq} \cos(k_{xm''}) \sin(k_{yn''}) dx'' dy''$.

Equations (37) and (38) can be written in the form of the matrix equation

$$\begin{bmatrix} Y_{pp'q'}^{aa} & Y_{pp'q'}^{ab} \\ Y_{pp'q'}^{ba} & Y_{pp'q'}^{bb} \end{bmatrix} \begin{bmatrix} A_{pq} \\ B_{pq} \end{bmatrix} = \begin{bmatrix} I_{xp'q'} \\ I_{yp'q'} \end{bmatrix} \quad (39)$$

Finally, we can solve the matrix Equation (39) to calculate the unknown coefficients A_{pq} and B_{pq} . Then, substituting A_{pq} and B_{pq} into the Equations (29)–(34), and the electromagnetic leakage fields outside the enclosure can be obtained.

In order to help understand the calculation process thoroughly, Figure 3 shows the flowchart of calculating the leakage fields in region III. Although we have ignored $E_{M_2}^{IIy}$ and $E_{M_2}^{IIx}$ when calculating M_{1x} and M_{1y} , this approximation works well for the problem.

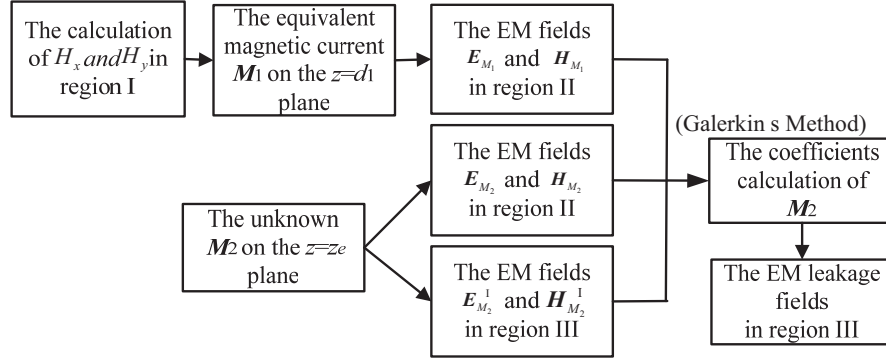


Figure 3. The flowchart of calculating the leakage fields in region III.

2.4. The Thickness of Aperture 2 is Finite

In fact, the enclosure wall often has a finite thickness which may directly influence the SE of the enclosure. Therefore, we can get a more precise result by taking the finite wall thickness into account. Based on Figure 1, Figures 4(a) and (b) respectively show the geometry of the enclosures and its side view when the thickness of the aperture 2 is infinite of d_2 . Region IV is volume inside the aperture 2

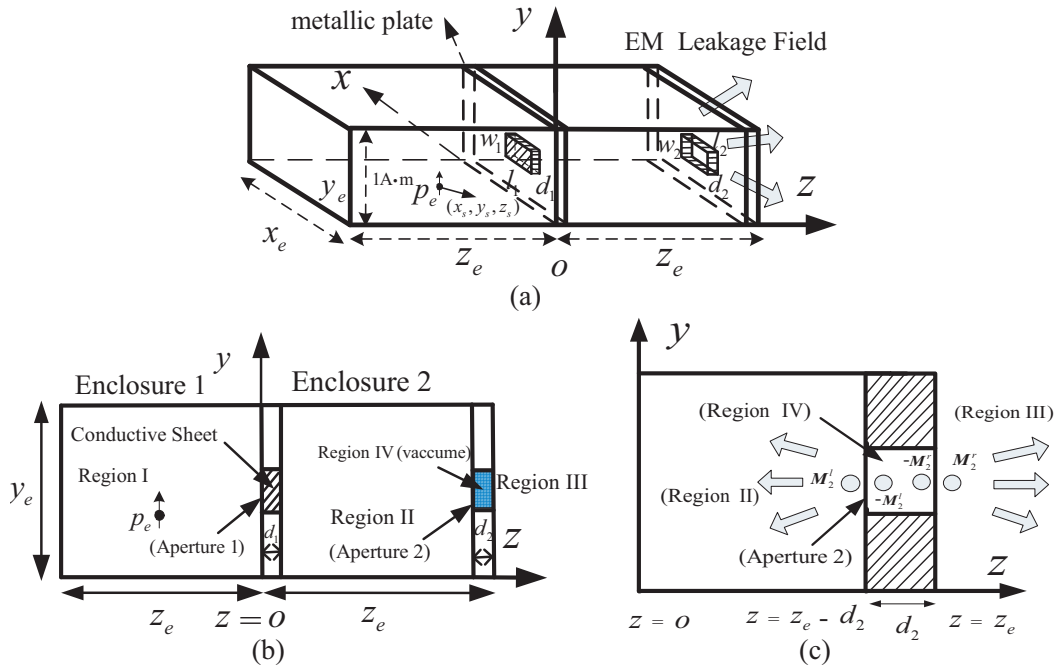


Figure 4. (a) Geometry of the enclosures when the thickness of aperture 2 is finite. (b) The corresponding side view of (a). (c) Equivalent magnetic currents M_2^l and M_2^r at both sides of aperture 2.

as shown in Figure 4(b).

In order to calculate the leakage field in region III, we represent the aperture 2 on $z = z_e - d_2$ plane and $z = z_e$ plane with the surface equivalent magnetic currents M_2^l and M_2^r respectively, shown as in Figure 4(c). In this case, the total leakage field in region II is the sum of the radiated fields from M_1 and M_2^l , and the total field in region IV is the sum of the radiated fields from $-M_2^l$ and $-M_2^r$, and the total field in region III is from the radiated field M_2^r . Similar to Section 2.3, by applying the continuity of tangential magnetic field at both sides of the aperture 2 and calculating the integral equations in the form of matrix based on the generalized model MoM, we can finally obtain the components M_{2x}^l , M_{2y}^l , M_{2x}^r , M_{2y}^r and therefore the leakage field in region III.

2.5. Aperture 2 is Covered by a Non-magnetic Conductive Sheet

Actually, the aperture 2 can also be covered by a non-magnetic conductive sheet 2 in order to improve the SE and suppress the electromagnetic leakage further. Based on Figure 4, Figures 5(a) and (b) respectively show the geometry of the enclosures and its side view when the aperture 2 is also covered by a sheet 2 of thickness d_2 , conductivity σ_2 , electric permittivity ε_0 and magnetic permeability μ_0 .

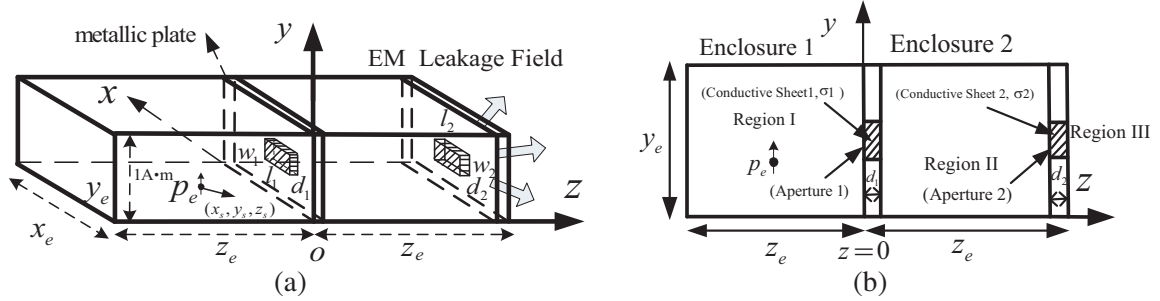


Figure 5. (a) Geometry of the hybrid model when aperture 2 is also covered by a non-magnetic conductive sheet 2. (b) The corresponding side view of (a).

In order to predict the electromagnetic leakage fields in region III through the two covered apertures, we should first calculate the electric vector potential A_{m2}^{III} according to Equation (5)

$$A_{m2}^{III} = \frac{\varepsilon_0}{4\pi} \iint_S \frac{M_3(r'') e^{-jk_0|r-r''|}}{|r-r''|} ds'' \quad (40)$$

where S'' denotes the area where sheet 2 covers, and $M_3(r'')$ is the equivalent magnetic current of the right surface of the sheet 2, which has both the x - and y -components.

According to Equations (12) and (13), the x -component and the y -component of $M_3(r'')$ are respectively obtained as

$$M_{3x} = 2E_{ty}^{III} = 2H_{M_1}^{IIx} \eta(d_2) \quad (41)$$

$$M_{3y} = -2E_{tx}^{III} = -2H_{M_1}^{IIy} \eta(d_2) \quad (42)$$

Therefore, we can obtain the leakage electric fields in region III by the light of Equation (5) as

$$E_{M_3}^{IIIx} = \frac{-1}{4\pi} \iint_S \frac{e^{-jk_0|r-r''|}(1+jk_0|r-r''|)}{|r-r''|^3} (z-z'') M_{3y}(r'') ds'' \quad (43)$$

$$E_{M_3}^{IIIy} = \frac{-1}{4\pi} \iint_S \frac{e^{-jk_0|r-r''|}(1+jk_0|r-r''|)}{|r-r''|^3} (z-z'') M_{3x}(r'') ds'' \quad (44)$$

$$E_{M_3}^{IIIz} = \frac{1}{4\pi} \iint_S \frac{e^{-jk_0|r-r''|}(1+jk_0|r-r''|)}{|r-r''|^3} [(x-x'') M_{3y}(r'') - (y-y'') M_{3x}(r'')] ds'' \quad (45)$$

It should be noted that we have ignored the tangential magnetic fields $H_{M_{3l}}^{IIx}$ and $H_{M_{3l}}^{IIy}$ in enclosure 2 generated by the magnetic current M_{3l} on the left surface of sheet 2 when calculating E_{ty}^{III} and E_{tx}^{III}

in Equations (41) and (42), but the approximation works well for the problem. This is due to when aperture 2 is also covered by a conductive sheet 2, the fields in region III decrease notably compared with the case that it is not covered. As a result, M_{3l} is much smaller, and the corresponding $H_{M_{3l}}^{IIx}$ and $H_{M_{3l}}^{IIy}$ are much smaller than the tangential magnetic fields $H_{M_1}^{IIx}$ and $H_{M_1}^{IIy}$ generated by the magnetic current M_1 on the right surface of sheet 1.

3. THE VALIDATION AND ANALYSIS OF THE HYBRID MODEL

In this section, the SE of the observation point is calculated by using the hybrid model proposed in Figure 1 for the intermediate analysis of the leakage field in region III. Since the electric dipole is oriented along the y -axis in the model, the y component dominates among the three electric field components, and we only consider E_y^{III} in calculating the SE. In order to verify these models, our results are compared with those from a full-analysis commercial software CST based on the TLM technique in the frequency range $0.1 \sim 3$ GHz respectively.

It is assumed that dimensions of enclosure 1 and 2 are both $300 \text{ mm} \times 120 \text{ mm} \times 300 \text{ mm}$, and the wall thickness of them is $t = 0.1 \text{ mm}$. Size of aperture 2 is $l_2 \times w_2 = 30 \times 20 \text{ mm}$. The electric dipole has a moment of $I \cdot dl = 1 \text{ A} \cdot \text{m}$, and located at $(152.5, 20, -147.5) \text{ mm}$. The center point of aperture 1 and 2 are located at $(150, 60, 0.5) \text{ mm}$ and $(150, 60, 300) \text{ mm}$, respectively. The observation point of SE is located at $(150, 60, 450) \text{ mm}$.

First, we consider a rectangular aperture 1 (Figure 6(a)) of length $l_1 = 50 \text{ mm}$ and width $w_1 = 40 \text{ mm}$ covered by a conductive sheet 1 of thickness $d_1 = 1 \text{ mm}$ and conductivity $\sigma_1 = 100 \text{ S/m}$. Then, we consider a covered square annular aperture 1 (Figure 6(b)) of which the outer size is $l_{b1} \times w_{b1} = 50 \times 50 \text{ mm}$, and the inner size is $l_{a1} \times w_{a1} = 20 \times 20 \text{ mm}$, and sheet 1 thickness is also $d_1 = 1 \text{ mm}$.

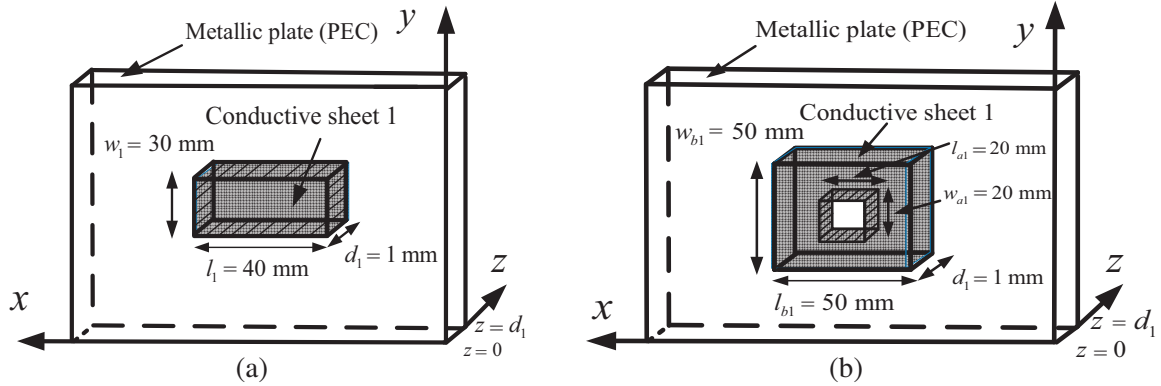


Figure 6. (a) The geometry of a $50 \text{ mm} \times 40 \text{ mm}$ rectangular aperture 1 covered by a conductive sheet 1 of thickness $d_1 = 1 \text{ mm}$. (b) The geometry of a square annular aperture 1 (outer size $50 \times 50 \text{ mm}$ and inner size $20 \times 20 \text{ mm}$) covered by a conductive sheet 1 of thickness $d_1 = 1 \text{ mm}$.

Figures 7(a) and (c) show the comparison of SEs of rectangular aperture 1 using the hybrid model and the results from the CST for different sheet conductivities $\sigma_1 = 100 \text{ S/m}$ and 10 S/m , respectively. It can be seen that the two curves are in good agreement up to 3 GHz in both figures. There are minimum values where the SEs decrease sharply due to the enclosure resonance effect. Frequencies of resonances f_{mnl} can be calculated by the following equation

$$f_{mnl} = \frac{1}{\sqrt{\mu_0 \epsilon_0}} \sqrt{\left(\frac{m}{2x_e}\right)^2 + \left(\frac{n}{2y_e}\right)^2 + \left(\frac{l}{2z_e}\right)^2} \quad (46)$$

where m , n , and l denote the resonance mode index numbers.

In our results all resonance modes have been identified corresponding to Equation (46), including the TM_{101} resonance at 0.71 GHz , the TM_{102} resonance at 1.12 GHz , the TM_{103} resonance at 1.58 GHz ,

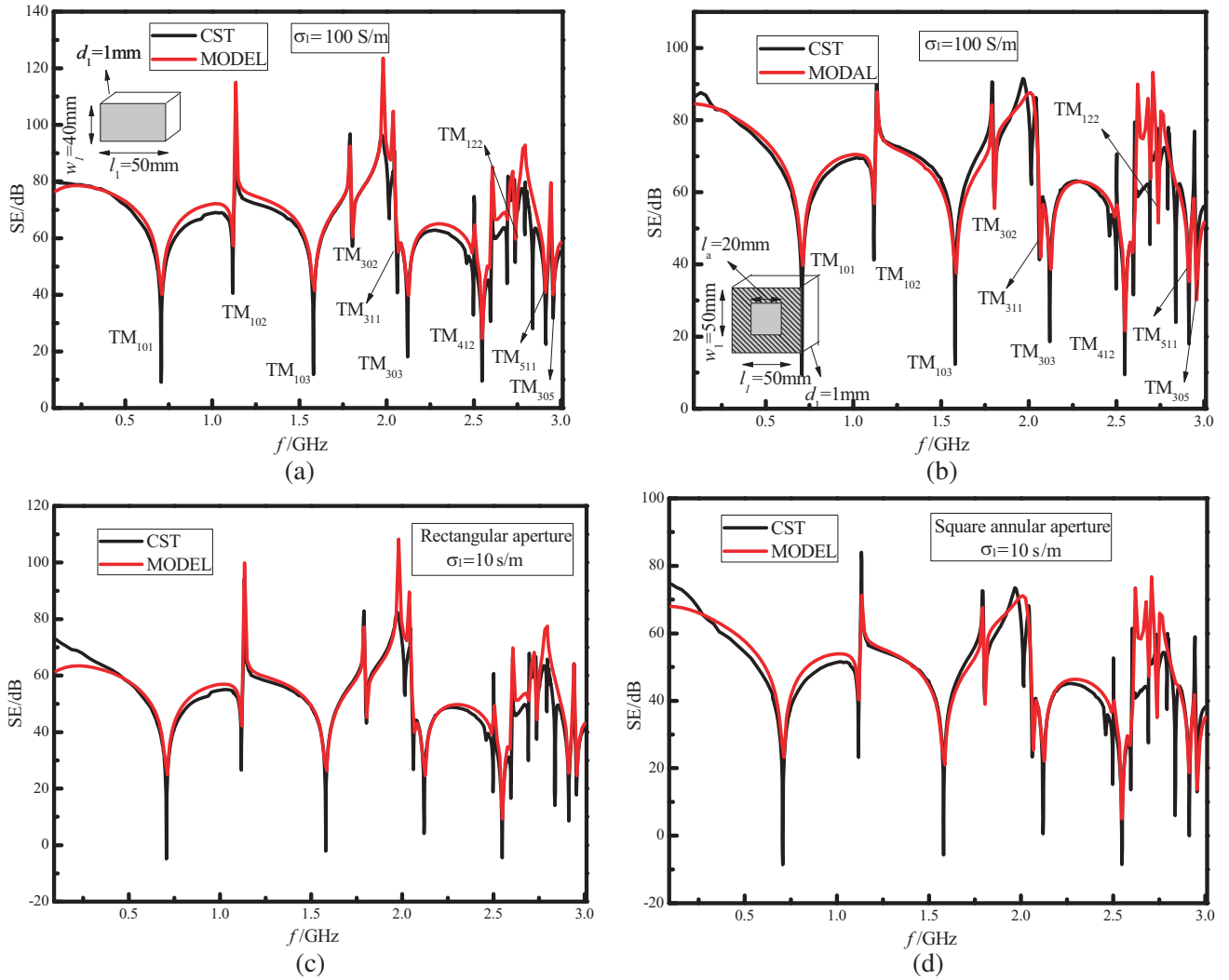


Figure 7. Comparison of SEs using the hybrid model and the results from the CST for (a) rectangular aperture 1 with sheet conductivity $\sigma_1 = 100$ S/m, (b) square annular aperture 1 with sheet conductivity $\sigma_1 = 100$ S/m, (c) rectangular aperture 1 with sheet conductivity $\sigma_1 = 10$ S/m, (d) square annular aperture 1 with sheet conductivity $\sigma_1 = 10$ S/m.

the TM_{302} resonance at 1.80 GHz, the TM_{311} resonance at 2.02 GHz, the TM_{303} resonance at 2.12 GHz, the TM_{412} resonance at 2.56 GHz, the TM_{122} resonance at 2.73 GHz, the TM_{511} resonance at 2.83 GHz, and the TM_{305} resonance at 3.91 GHz. At the same time, we can see there are maximum values where the SEs increase sharply on account of the standing-wave's zero effect, which can be attributed to the following two main possible reasons, one is that the electric dipole is at the position where the E_y^{III} is zero, which makes the coupling between the source and the leakage field very weak; the other is that aperture 1 is at the position where the H_x^I is zero, and the equivalent magnetic current M_1 only has the M_{1x} component ($M_{1x} = 2\eta(d_1)H_x^I$), which makes M_1 zero, and thus the leakage fields reduce greatly accordingly.

Figures 7(b) and (d) show the comparison of SEs of the square annular aperture 1 using the hybrid model and the results from the CST for different sheet conductivities $\sigma_1 = 100$ S/m and 10 S/m, respectively. It can be seen that the two curves are in good agreement within most of the frequency range up to 3 GHz in both figures, indicating that the hybrid model proposed is not limited to the general rectangular apertures. This limitation is eliminated by replacing the right surface of the covered

aperture 1 with equivalent magnetic current, and thus we only need to change the area the sheet 1 covers in calculating its contribution to the electromagnetic leakage fields in region II for different aperture shapes. Except for the rectangular and square annular aperture, the hybrid model can also handle other cases including the circular and the elliptical aperture or the combinations of these shapes.

There are accurate and efficient advantages when using the hybrid model to solve the electromagnetic leakage problem from the apertured complex enclosures. All the computations are completed on the same computer with the CPU for Intel® Core (TM) I5-4200 M @3.1 GHz and 8 GB memory, the CST consumes about 25129 s completing the simulation while the hybrid model consumes only about 282 s on average. It is found that the calculation speed of the hybrid model improves about 88 times. This comparison concludes that the proposed model performs better efficiency without sacrificing much calculation accuracy.

In the following discussion, we focus on the case that aperture 1 is rectangular, and analyze respectively the thickness and the conductivity of sheet 1 on the leakage field in region III by using the verified hybrid model. Figure 8(a) shows the SEs calculated for different sheet 1 thicknesses of $d_1 = 2$ mm, 3 mm and 4 mm. Figure 8(b) shows the SEs calculated for different sheet 1 conductivities of $\sigma_1 = 30$ S/m, 50 S/m and 70 S/m. It can be seen that the larger the thickness and the conductivity of sheet 1 are, the higher the SEs are, and the less the electromagnetic leakage field in region III. The reason is that when other parameters keep unchanged, the leakage field in region II is determined by the function $|\eta(d_1)|$ according to Equations (16)–(21), which is a monotonic decreasing function, as is shown in Figures 9(a) and (b) which describe the variations of absolute value $|\eta(d_1)|$ with the frequency change for different thicknesses and conductivities of sheet 1. From the Equations (8) and (10), it can also be seen that the equivalent magnetic current M_1 is related to the function $|\eta(d_1)|$ ($M_1 = 2\eta(d_1)H_x^I e_x$). Therefore, with the increase of the value of sheet 1 thickness or its conductivity, the value of function $|\eta(d_1)|$ decreases, and then the absolute value of M_1 reduces, leading to less leakage field in region II, finally there is a decrease of the leakage field in region III.

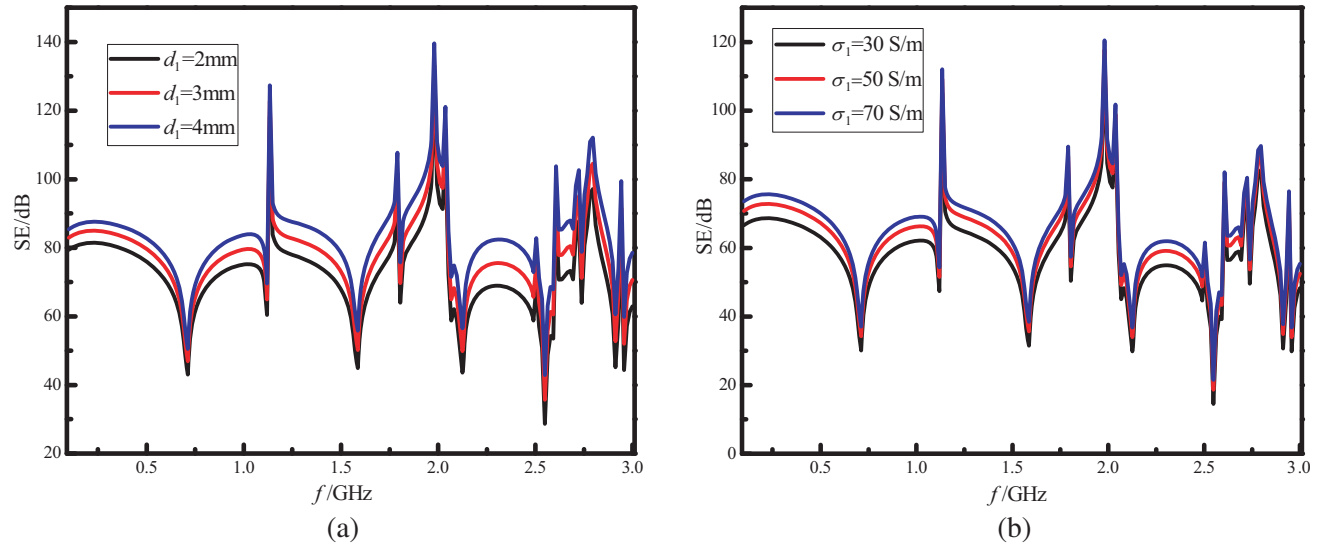


Figure 8. Variations of SEs calculated with the frequency change for (a) three different sheet 1 thicknesses $d_1 = 2$ mm, 3 mm, 4 mm, (b) three different sheet 1 conductivities $\sigma_1 = 30$ S/m, 50 S/m, 70 S/m.

In order to reflect the relation between the SEs versus thickness and conductivity of sheet 1, Figures 10(a) and (b) show the variations of the SEs calculated at three resonant frequencies (0.71 GHz, 1.58 GHz and 2.12 GHz) with respect to thickness and conductivity of sheet 1, respectively. From Figures 10(a) and (b), we can clearly see that with the increase of the thickness and conductivity values, the SEs increase accordingly.

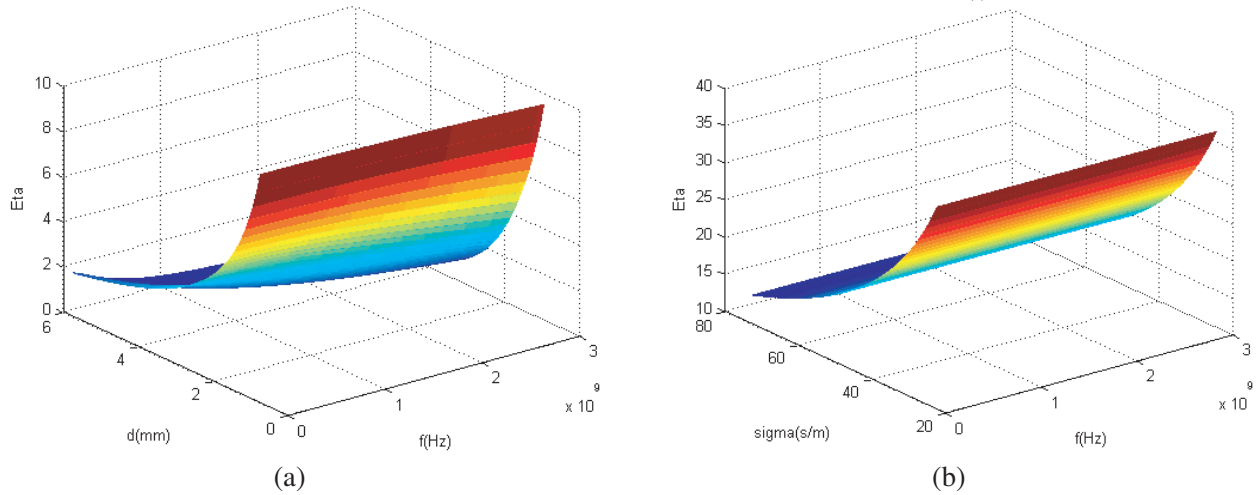


Figure 9. Variations of absolute value $|\eta(d_1)|$ calculated with frequency change for (a) different sheet 1 thicknesses, (b) different sheet 1 conductivities.

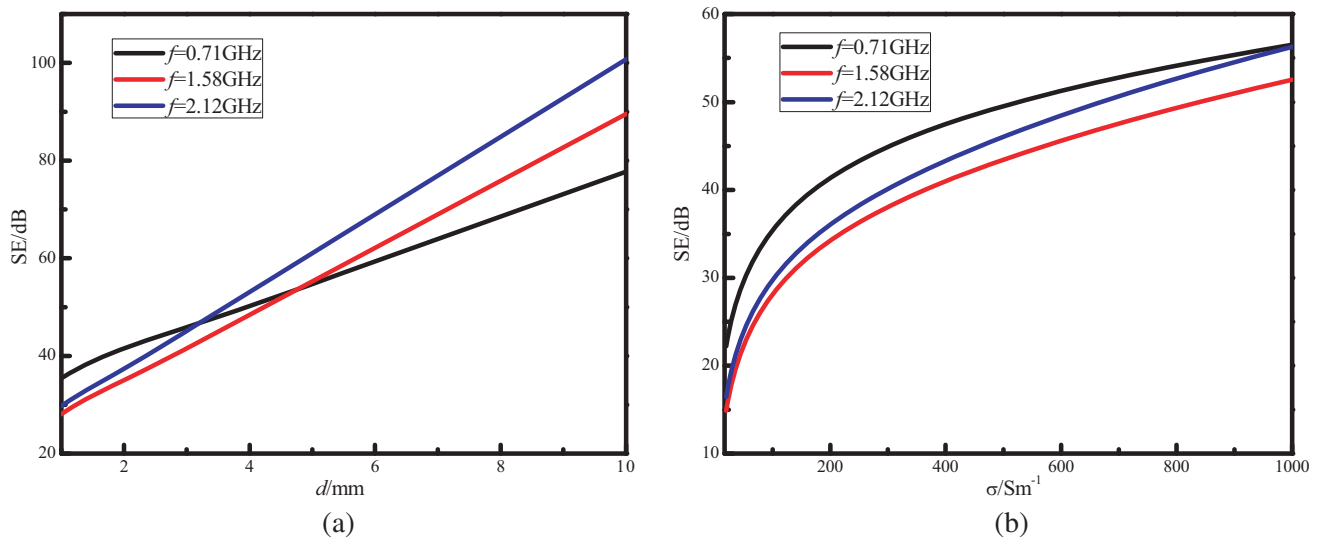


Figure 10. Variations of the SEs calculated at three resonant frequencies with (a) sheet 1 thickness d_1 , (b) sheet 1 conductivity σ_1 .

4. ELECTROMAGNETIC LEAKAGE UNDER DIFFERENT CONDITIONS USING THE HYBRID MODEL

4.1. The Metallic Plate is Made of Conductive Material without Apertures

Figures 11(a) and (b) respectively show the geometry and side view of the enclosures in the case of the whole plate in the middle, which is made of non-magnetic conductive material without apertures. Keeping other parameters unvaried, the plate conductivity is $\sigma_1 = 100 \text{ S/m}$ and the thickness $d_1 = 1 \text{ mm}$. Figure 12 shows the comparison of SEs using the hybrid model and the results from the CST. It can be seen that the hybrid results are in good agreement with those from the CST. Compared with the case of Figure 1, there are three differences: 1) the SEs in Figure 11 decrease in the whole frequency range, because the shielding effect in this case is much poorer than that of the perfect metallic conductor. 2) Some resonance modes disappear, such as resonances TM_{302} , TM_{511} and TM_{122} . The reason is that the

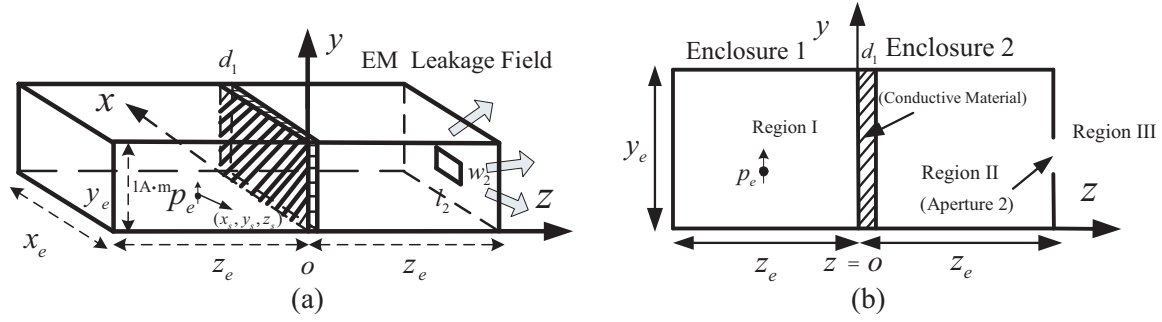


Figure 11. (a) Geometry of the enclosures when the whole plate between enclosure 1 and enclosure 2 is made of non-magnetic conductive material without apertures. (b) The corresponding side view of (a).

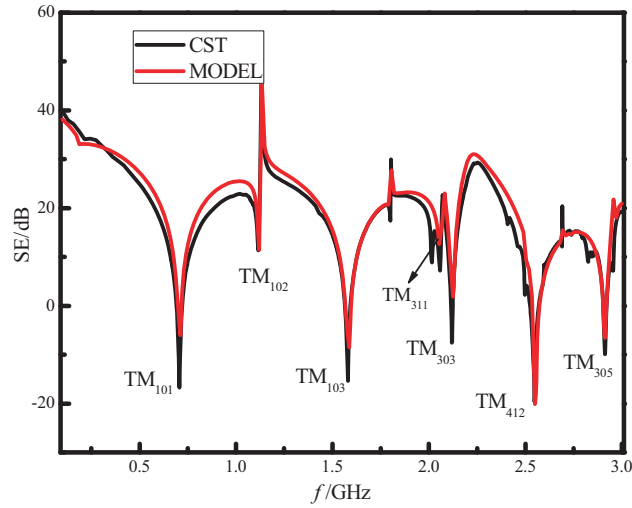


Figure 12. Comparison of SEs using the hybrid model and the results from the CST when the whole plate in the middle is made of non-magnetic conductive material without apertures.

electric field component E_y^{III} in the frequencies corresponding to these resonances is zero in the position of the electric dipole, and thus these vanished modes cannot be inspired. 3) There are no maximum values in some frequency ranges such as 1.8 ~ 2.1 GHz and 2.5 ~ 2.9 GHz, and the reason that the SEs do not increase sharply is that the zero effect of standing-wave is suppressed greatly in these frequency ranges. When the whole plate is composed of non-magnetic conductive material without apertures, the equivalent magnetic current on the $z = d_1$ plane increases greatly, which causes an increase of the leakage field in region II and region III, and thus the coupling between the dipole and the electromagnetic modes is enhanced.

4.2. The Thickness of Aperture 2 Is Finite

In the case of Figure 4, rectangular aperture 2 is finite with thickness $d_2 = 5$ mm, and other parameters kept unvaried.

The SEs respectively obtained from our model and the CST are compared in Figure 13(a). It can be seen that the two curves present good agreement in most of the frequency range up to 3 GHz. Figure 13(b) shows the comparison of SEs calculated for the cases in Figure 1 and Figure 4, and it can be seen that the SEs increase notably as the aperture thickness is added to 5 mm.

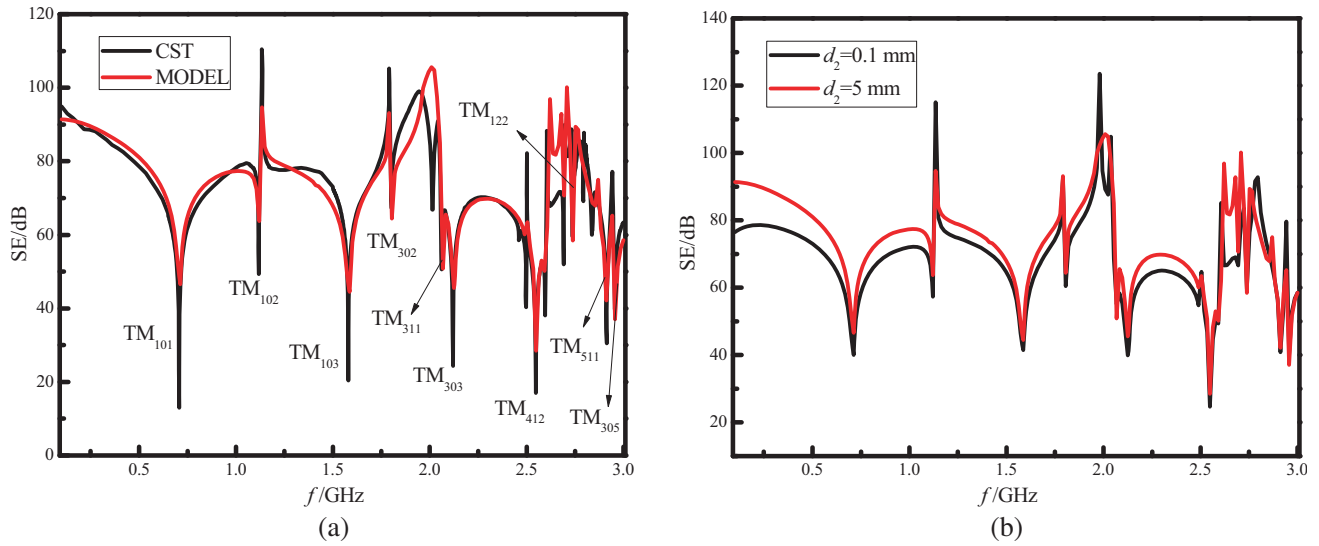


Figure 13. (a) Comparison of SEs using the hybrid model and the results from the CST when the thickness of aperture 2 is infinite. (b) Comparison of SEs calculated when aperture 2 thickness is $d_2 = 0.1$ mm and $d_2 = 5$ mm.

4.3. Aperture 2 Is Covered by a Non-Magnetic Conductive Sheet

In the case of Figure 5, aperture 2 is covered by a non-magnetic conductive sheet 2 of thickness $d_2 = 1$ mm and conductivity $\sigma_2 = 100$ S/m. Figure 14(a) shows the comparison of SEs using our model and the results from the CST. It can be seen that the two curves are in good agreement in most of the frequency range up to 3 GHz. At the same time, we also give the comparison of cases in Figure 1 and Figure 5, as depicted in Figure 14(b). It can be seen that the SEs in the case of Figure 5 are higher than that of the case of Figure 1, especially in the frequency range 2.1 ~ 2.5 GHz, indicating that the electromagnetic leakage to the outside decreases apparently when aperture 2 is also covered by conductive sheet 2.

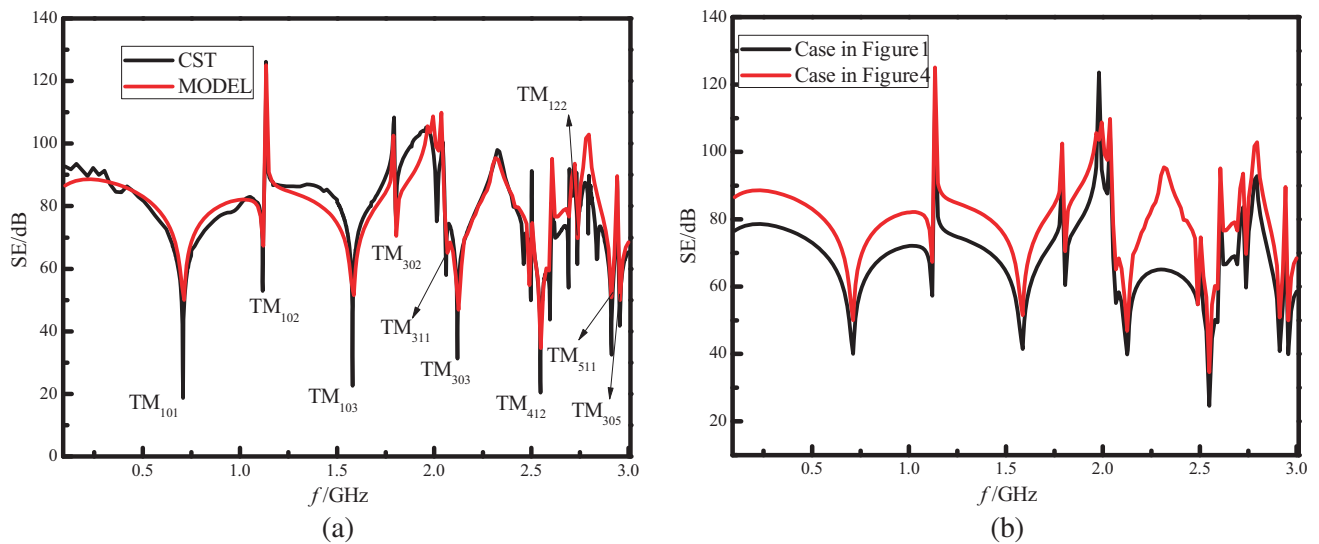


Figure 14. (a) Comparison of SEs using our model and the results from the CST when aperture 2 is also covered with a conductive sheet 2. (b) Comparison of SEs calculated when aperture 2 is covered by a conductive sheet 2 or not.

5. CONCLUSION

In this paper, an efficient and accurate hybrid model has been developed to predict the electromagnetic leakage field from complex metallic enclosures through apertures covered by a conductive sheet using the SE as the measurement of the leakage field. First, we use the dyadic Green's function and the boundary condition of a sheet with infinite extension against a plane wave of normal incidence in order to derive the leakage fields excited by an internal electric dipole. Then, we derive the leakage fields outside the enclosure based on the generalized MoM. All the results calculated by the hybrid model are in good agreement with those from the full-wave simulation software CST within broad frequency range up to 3.0 GHz. At the same time, the model is employed to analyze the effect of different factors on the SE, including the thickness and conductivity of the sheets. Results show both of the thickness and conductivity have a significant influence on the amplitude of the SE; the larger the thickness and the conductivity are, the higher the SE is, and thus the less the leakage field is. Finally, the hybrid model is extended to handle other cases, including the whole plate made of conductive material without apertures, finite thickness of the aperture at the end of the enclosure and the aperture at the end of the enclosure covered by a conductive sheet. Results show that the electromagnetic leakage field is the most for the first case, while for the other two cases the shielding effect is much better than the case that the thickness of the aperture at the end of the enclosure is a very small value, indicating that the electromagnetic leakage field is suppressed effectively.

ACKNOWLEDGMENT

The authors thank for the funding support from the National Natural Science Foundation (No. 61372050) and the Fundamental Research Funds for the Central Universities in China (Grant No. 2016MS06).

REFERENCES

1. Paul, C. R., *Introduction to Electromagnetic Compatibility*, 2nd Edition, John Wiley & Sons Inc, New Jersey, USA, 2006.
2. Henry, W. O., *Electromagnetic Compatibility Engineering*, 1st Edition, Wiley Interscience, New York, USA, 2009.
3. Gomory, F., M. Solovyov, J. Souc, et al., "Experiment realization of a magnetic cloak," *Science*, Vol. 335, No. 6075, 1466–1468, 2012.
4. Araneo, R. and G. Lovat, "An efficient MoM formulation for the evaluation of the shielding effectiveness of rectangular enclosures with thin and thick apertures," *IEEE Trans. Electromagn. Compat.*, Vol. 50, No. 2, 294–304, 2008.
5. Robinson, M. P., T. M. Benson, C. Christopoulos, et al., "Analytical formulation for the shielding effectiveness of enclosures with apertures," *IEEE Trans. Electromagn. Compat.*, Vol. 40, No. 240, 240–248, 1998.
6. Hao, J.-H., P.-H. Qi, J.-Q. Fan, and Y.-Q. Guo, "Analysis of shielding effectiveness of enclosures with apertures and inner windows with TLM," *Progress In Electromagnetic Research M*, Vol. 32, 73–82, 2013.
7. Tharf, M. S. and G. I. Costache, "A hybrid finite element-analytical solutions for in-homogeneously filled shielding enclosures," *IEEE Trans. Electromagn. Compat.*, Vol. 36, No. 4, 380–385, 1994.
8. Bethe, H. A., "Theory of diffraction by small holes," *Phy. Rev. II*, Vol. 66, Nos. 7 and 8, 163–182, 1944.
9. Nitsch, J., S. Tkachenko, and S. Pottast, "Pulsed excitation of resonators," *Interaction Note*, Note 619.
10. Anderieu, G., J. Panh, A. Reineix, P. Pelissou, et al., "Homogenization of composite panels from a near-field magnetic shielding effectiveness measurement," *IEEE Trans. Electromagn. Compat.*, Vol. 54, No. 3, 700–703, 2012.

11. Chen, M.-D., X.-H. Xie, and H.-Y. Zhang, "Simulation and calculation of the absorbing microwave properties of carbon nanotube composite coating," *Acta Physica Sinica*, Vol. 63, No. 6, 0661031–0661036, 2014.
12. Jiao, C.-Q., "Shielding effectiveness improvement of metallic waveguide tube by using wall losses," *IEEE Trans. Electromagn. Compat.*, Vol. 54, No. 3, 696–699, 2012.
13. Konefal, T., J. F. Dawson, A. C. Martin, et al., "A fast circuit model description of the shielding effectiveness of a box with imperfect gaskets or apertures covered by thin resistive sheet coatings," *IEEE Trans. Electromagn. Compat.*, Vol. 48, No. 1, 134–144, 2006.
14. Tesche, F. M., M. V. Ianoz, and T. Karlsson, *EMC Analysis Methods and Computational Models*, 1st Edition, Wiley Inter Science, New York, USA, 1996.
15. Deshpande, M. D., "Electromagnetic field penetration studies," *NASA Technical Paper*, June 2000.
16. Jiao, C.-Q. and Y.-Y. Li, "Reciprocity principled-based model for shielding effectiveness prediction of a rectangular cavity with a covered aperture," *Chinese Physics B*, Vol. 24, No. 10, 1041011–1041016, 2015.
17. Dehkhoda, P., A. Tavakoli, and R. Moini, "Shielding effectiveness of a rectangular enclosure with finite wall thickness and rectangular apertures by the generalised modal method of moments," *IET Science, Measurement and Technology*, Vol. 3, No. 2, 123–136, 2009.
18. Khan, Z. A., C. F. Bunting, M. D. Deshpande, et al., "Validation of Modal/MoM in shielding effectiveness studies of rectangular enclosures with apertures," *IEEE Trans. Electromagn. Compat.*, Vol. 48, No. 2, 348–353, 2006.